Road Crack Detection and Orientation Estimation Using Airborne Synthetic Aperture Radar

Arun Babu, *Graduate Student Member, IEEE*, Stefan V. Baumgartner, *Senior Member, IEEE*, and Gerhard Krieger, *Fellow, IEEE*

***Abstract*—Cracks on road surfaces are a significant safety hazard that can progress into larger potholes, posing risks to vehicles and passengers. Synthetic aperture radar (SAR) data acquired by high-resolution airborne SAR systems are sensitive to changes on the road surface and can be utilized for periodic road condition monitoring. This study proposes a novel method that combines an adaptive thresholding algorithm with the Radon transform for detecting road cracks and estimating both their severity and orientation. In this approach, the adaptive thresholding algorithm detects the cracks, while the Radon transform qualitatively quantifies their severity using the maximum Radon magnitude from the sinogram and estimates their orientation as bearing angles relative to true north. While the proposed method is applicable to various airborne SAR platforms, it is demonstrated in this study with X-band airborne SAR data acquired by DLR's F-SAR system with a spatial resolution of 25 cm. The detected cracks and orientations were validated against Google Earth images, showing close agreement with the locations and orientations of the actual cracks. This research underscores the potential of airborne SAR data in supporting predictive road maintenance efforts through early identification of surface defects.**

***Index Terms*—Synthetic aperture radar, airborne radar, surface cracks, thresholding, transforms, vehicle safety.**

I. Introduction

ROAD surfaces with cracks and potholes pose significant safety risks to vehicles, leading to accidents and premature vehicle wear and tear [1]–[4]. Road cracks form due to a variety of reasons, including repetitive loading from heavy vehicles [5], defects due to construction methods and materials [6], subgrade instability [7], moisture ingress [8], and temperature-induced expansion and contraction [9]–[11]. In cold climates, the freeze-thaw cycles during winter further accelerate the crack and pothole formation [12], [13]. During these cycles, melted snow seeps into existing small road cracks, freezes, expands, and further widens them. As temperatures rise again, the ice melts and leaves voids beneath the road surface, which collapse under traffic loads, forming potholes, as illustrated in Fig. 1.

Given the critical importance of ensuring road safety, periodic monitoring of road conditions is essential for carrying out maintenance activities. In several countries, road condition monitoring is carried out using specialized survey vehicles equipped with several sensors including ground penetrating radar (GPR) and laser crack measurement system (LCMS),

Arun Babu, Stefan V. Baumgartner, and Gerhard Krieger are with the Microwaves and Radar Institute, German Aerospace Center (DLR), 82234 Weßling, Germany (email: arun.babu@dlr.de; stefan.baumgartner@dlr.de; gerhard.krieger@dlr.de).

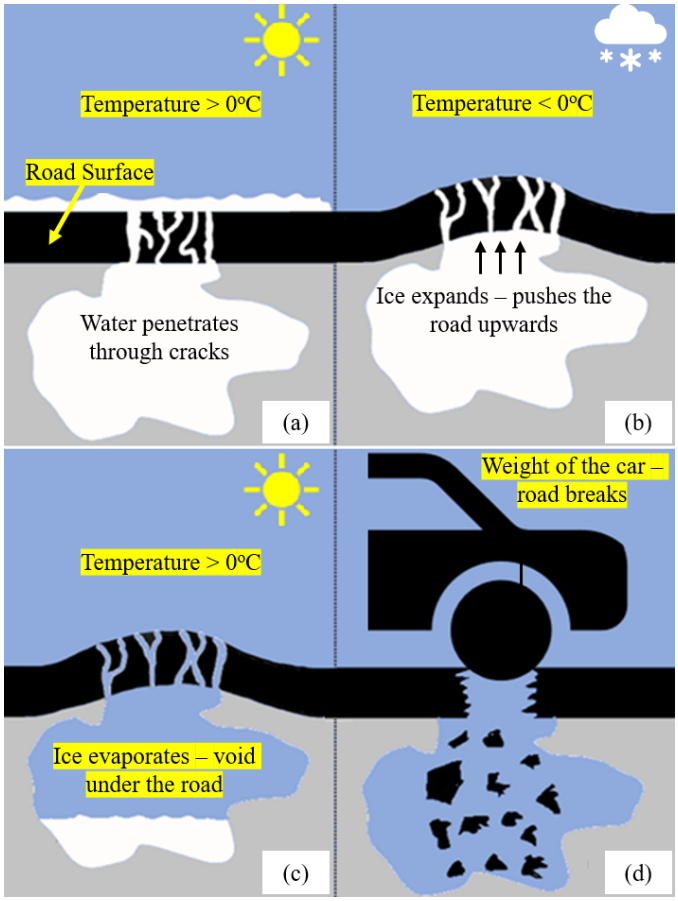

Fig. 1. Cracks deterioration and pothole formation due to freeze-thaw cycles in the winter season.

which can detect various types of road cracks, including longitudinal, transverse, and alligator cracking [14], [15]. However, these surveys are costly, time-consuming, and labor-intensive, which limits their frequency and scope [16]. For example, in Germany, such surveys are carried out in average only every four years, with a focus only on the major motorways [17]. Considering the rapid deterioration of the road surfaces, especially in winter, there is an increasing demand for more frequent monitoring of road conditions, ideally annually [18]. Regular monitoring would enable early detection of road deterioration, facilitating predictive maintenance strategies and reducing the risks to road users.

To address these challenges, remote sensing techniques have been widely considered as a time and cost-efficient approach

for large-scale road condition monitoring [19]. However, most prior studies available in the literature rely on high-resolution optical images acquired using unmanned aerial vehicles (UAVs) or vehicle-mounted cameras. These optical methods employ either classical image processing techniques (e.g., edge detection, texture analysis, thresholding, morphological operations) or deep learning models such as convolutional neural networks (CNNs) and semantic segmentation networks for road crack detection [20]–[23]. While these techniques have demonstrated promising results, their performance is often hindered by variations in illumination, shadows, surface stains, and other environmental conditions [23]. Moreover, the reliance on UAV or vehicle-mounted imaging platforms restricts the spatial coverage of these approaches to localized inspections only.

SAR offers a promising alternative for road condition monitoring due to its active sensing nature, which allows operation regardless of the ambient lighting, and it is also very sensitive to changes on the road surface [24]. That said, studies in the existing literature have focused on the estimation of road unevenness and general road damage detection using medium-resolution spaceborne SAR data [25]–[27]. Previous research at the German Aerospace Center (DLR) has demonstrated the successful generation of road surface roughness images using high-resolution airborne and spaceborne X-band SAR data from DLR's F-SAR and Germany's TerraSAR-X (TS-X) systems, respectively [16], [28], [29].

Building upon the previous research, this study proposes a novel method for detecting road cracks and estimating both their severity and orientation. To the best of our knowledge, no prior study has demonstrated the detection, severity, and orientation of road cracks using high-resolution SAR images. The proposed method utilizes high-resolution surface roughness (h_{rms}) images generated from the airborne X-band F-SAR data as input [16]. The processing chain developed in this study combines an adaptive thresholding algorithm for crack detection with the Radon transform for subsequent severity and orientation estimation. Detecting cracks and estimating their orientation is crucial for understanding the causes behind their formation and taking appropriate corrective measures. For instance, longitudinal cracks that run parallel to the road are usually caused by large tensile stresses near the tire paths [30]. In contrast, transverse cracks that run perpendicular to the road are often due to problems such as soil settlement, shrinkage, improper joint spacing, or freeze-thaw cycles in winter [31], [32].

The remainder of this article is structured as follows: Section II provides an overview of the test site and the datasets used in this study. Section III introduces the proposed adaptive thresholding algorithm for crack detection. The methodology for estimating the crack severity and orientation using the Radon transform is detailed in Section IV. Section V discusses the experimental results, and Section VI concludes this article.

II. Test Site and Datasets

The primary test site considered for this study is the Kaufbeuren Airfield in Bavaria, Germany. This test site is

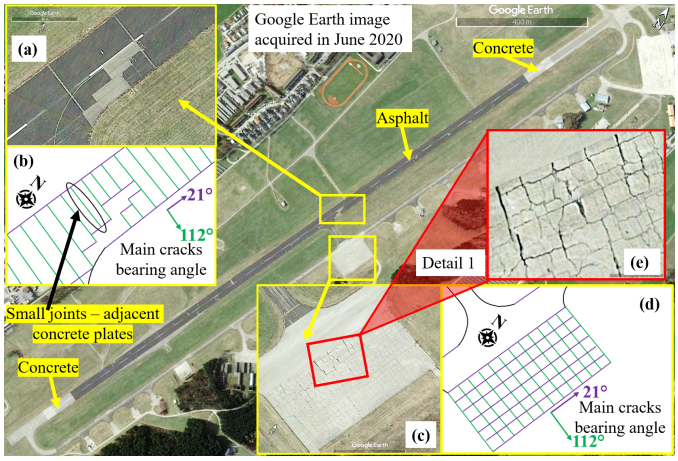

Fig. 2. Google Earth image of the entire Kaufbeuren airfield showing regions selected for this study. (a) Section of the runway. (c) Severely cracked parking area. (b) and (d) shows the expected crack images illustrating the main cracks present in these two regions and their bearing angles. (e) Zommed-in view of a section of the parking area.

a disused military airfield where no maintenance work has been carried out for several years. A Google Earth (GE) image acquired in June 2020 showing an overview of the entire airfield is depicted in Fig. 2. Two regions of the airfield with several cracks and potholes are selected for this study. The first region is a section of the runway, featuring repair patches and small joints between adjacent concrete plates beneath the asphalt layer (see GE image in Fig. 2(a)), and the second region is a severely cracked parking area shown in Fig. 2(c). Most cracks in these regions are found to have two orientations: longitudinal to the runway and transverse to the runway. The images with the expected cracks in these two regions are illustrated in Fig. 2(b) and (d), with purple lines indicating longitudinal cracks and green lines indicating transverse cracks. The actual bearing angles of these cracks w.r.t. true north are 21 degrees for the longitudinal cracks and 112 degrees for the transverse cracks. These two bearing angles are considered as the ground truth values for validating the crack orientations estimated from the airborne F-SAR data. It is important to note that the expected crack images depicted in Fig. 2(b) and (d) serve primarily as reference sketches intended to give an approximate idea of the crack locations and orientations. These were drawn based on careful visual inspection of high-resolution F-SAR and GE images. While Fig. 2(b) provides approximate positions and orientations of runway joints and patchwork edges on the runway, Fig. 2(d) depicts only the general orientations due to the complexity of several interconnected cracks in the parking area, making manual delineation of the individual cracks challenging. A zoomed-in section of the parking area, labeled 'Detail 1' and outlined by a red rectangle in Fig. 2(c), is selected for a more detailed analysis of the severe cracks and their orientations. The corresponding GE image of this area is shown in Fig. 2(e), and the results for this section are presented later in Section V.

Several X-band F-SAR datasets, each with a spatial resolution of $25\,\mathrm{cm} \times 25\,\mathrm{cm}$ (azimuth $\times$ range), were acquired over

the Kaufbeuren airfield on 04 September 2020 with various incidence and aspect angles relative to the runway. For this study, geocoded surface roughness (h_{rms}) images generated as part of the previous research [16] from the F-SAR dataset with ID 'PS04', with a flight track parallel to the runway, and the dataset 'PS05', with a flight track perpendicular to the runway, were considered as input for the crack detection and orientation estimation. Additionally, fused h_{rms} images, which are also generated as part of the previous research [16] by fusing h_{rms} images from multiple F-SAR datasets with varying acquisition geometries, using both multi-dataset averaging and highest signal-to-noise ratio (SNR) fusion methods, were also considered as input for this study. In the multi-dataset averaging method, the fused h_{rms} image is generated by the pixel-by-pixel averaging of the h_{rms} values estimated from multiple datasets. In the highest SNR method, a pixel-wise SNR search was done on all the datasets, and for each pixel, the h_{rms} value estimated from the dataset having the highest SNR was selected. In this method, the final h_{rms} image is generated only from the highest SNR pixels selected from all the available datasets. More information about the Kaufbeuren airfield, F-SAR datasets, and the fusion methods can be found in [16].

III. Windowed Adaptive Thresholding Algorithm for Cracks Detection

An adaptive thresholding algorithm is proposed in this study for performing the crack detection that operates on the geocoded h_{rms} image generated as part of the previous research [16]. A block diagram illustrating the algorithm is shown in Fig. 3. The h_{rms} image is chosen as the input image for performing the adaptive thresholding because it shows a sharp increase in h_{rms} values at the cracked regions compared to the surrounding smooth road surfaces (see example image shown in Fig. 3(a)). This relative increase is more pronounced than what is observed for the SAR backscatter (σ^o) values, which can potentially improve the performance of the adaptive thresholding algorithm in crack detection.

Since the h_{rms} image can contain high h_{rms} values originating from overhead signboards, metallic lane dividers, flyover walls, and other strong reflecting features, it is recommended to perform an upper σ^o thresholding on the h_{rms} image, as suggested in [16], before applying the adaptive thresholding algorithm for crack detection. This procedure masks out regions with backscatter values above typical road-surface levels, thereby preventing the adaptive thresholding algorithm from falsely detecting these high-backscattering non-road features as cracks. Once such strong reflecting targets are masked out, the remaining high surface roughness changes detected by the adaptive thresholding algorithm are more likely associated with actual road surface anomalies such as cracks, potholes, or material boundaries (e.g., asphalt-concrete joints), all of which should be flagged for further inspection by the road maintenance authorities.

The adaptive thresholding algorithm is applied locally to the input h_{rms} image using an N $\times$ N sliding window. For each window, the N $\times$ N h_{rms} values are first filtered with a median filter to reduce spikey noise that can interfere with accurate threshold estimation. The crack detection threshold (τ_i) for the i^{th} sliding window is then estimated as:

$$\tau_i = \mu_i + \sigma_i \ , \tag{1}$$

where μ_i and σ_i are the mean and standard deviation computed within the i^{th} sliding window.

The center pixel within a sliding window is classified as a crack if its h_{rms} value exceeds the computed threshold τ_i and is at least 1.2 mm (an empirically determined value for the X-band F-SAR data). Pixels satisfying these conditions are marked as cracks (value = 1) in the output image; otherwise, they are labeled as smooth (value = 0). This decision rule is mathematically expressed as:

$$\begin{array}{l}\text{Binary}\\ \text{crack}\\ \text{detection}\\ \text{output}\end{array} = \begin{cases} 1, & \text{if } h_{\mathrm{rms}}(i = \mathrm{N}/2,\, k = \mathrm{N}/2) \geq \tau_i \\ & \text{and } h_{\mathrm{rms}}(i = \mathrm{N}/2,\, k = \mathrm{N}/2) \geq 1.2 \\ 0, & \text{otherwise} \end{cases} \tag{2}$$

The resulting binary cracks detection map (cf. Fig. 3(b)) is then multiplied pixel by pixel with the input h_{rms} image, retaining h_{rms} values only for the cracked regions and setting the values in smooth regions to '0'. This resulting crack roughness image (cf. Fig. 3(c)) is then used as input to the Radon transform for estimating the severity and orientation of the cracks (refer to Section IV). For performing the N $\times$ N adaptive thresholding algorithm, it is necessary to choose a suitable window size so that the cracks can be accurately detected. After experimenting with different window sizes, a 25×25 sliding window is selected as the suitable window size for performing the adaptive thresholding.

It is also important to note that different road surface materials exhibit varying surface roughness characteristics. For instance, concrete generally displays higher h_{rms} values than asphalt due to the coarser grain structure of the materials used [16], [28], [29]. However, the adaptive thresholding algorithm proposed in this study does not rely on absolute roughness values but rather on detecting local anomalies, i.e., sudden variations in h_{rms} values within a localized window. Therefore, whether the surface is asphalt or concrete, a crack is identified only if it produces a significant change in roughness relative to the surrounding pixels. This makes the algorithm robust and effective across different pavement types.

IV. Windowed Radon transform for cracks severity and orientation estimation

The Radon transform is an integral transform widely used in fields such as medical imaging, including computed tomography (CT) and nuclear magnetic resonance (NMR) imaging [33]. It effectively captures oriented features in images by calculating line integrals along various directions [34], making it suitable for estimating the severity and orientation of road cracks. In this study, the Radon transform is investigated in two ways for crack severity and orientation estimation: first, it is applied to simulated road crack images, and second, a

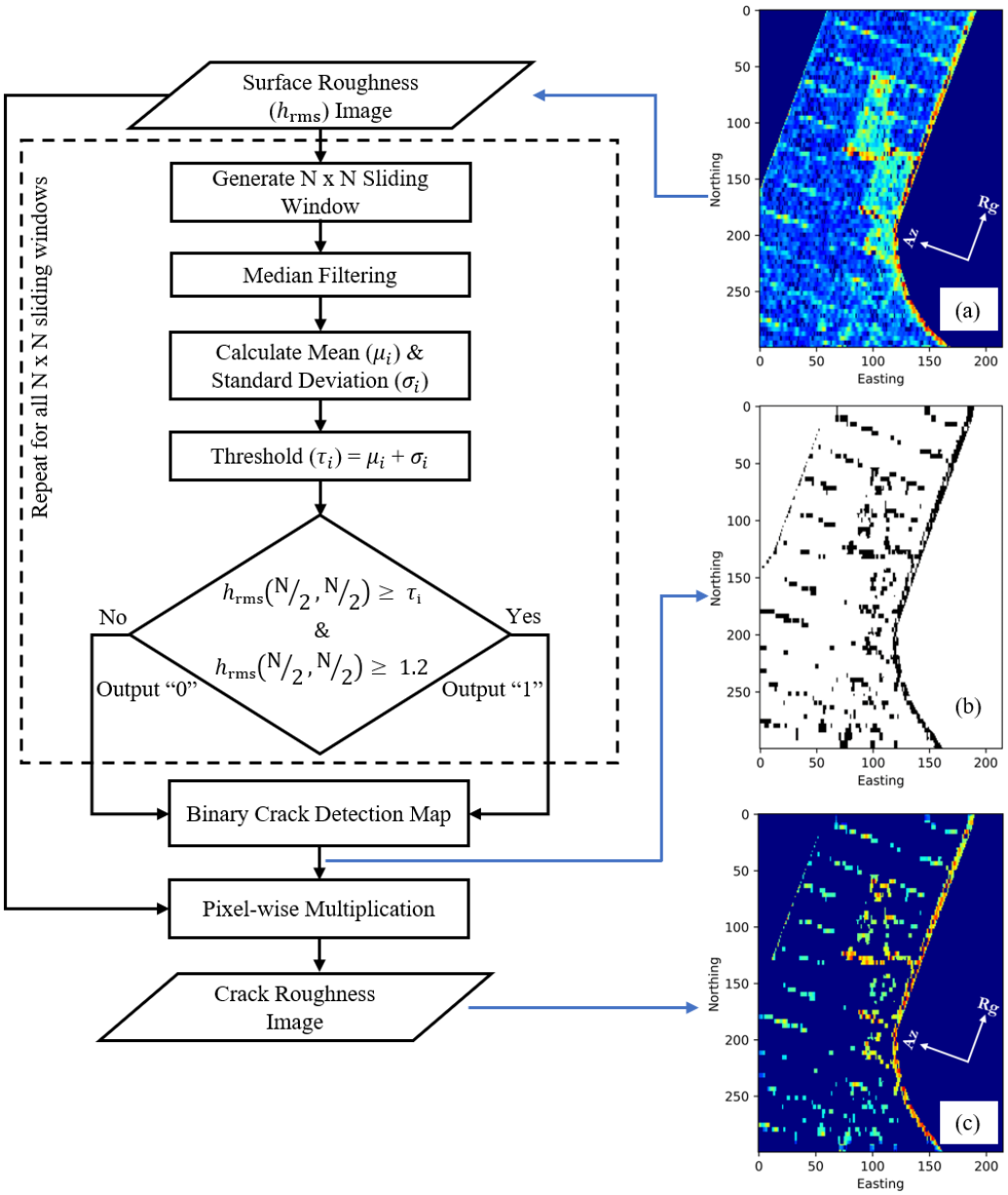

Fig. 3. Block diagram of the windowed adaptive thresholding algorithm for crack detection. (a) Input surface roughness (h_{rms}) image. (b) Output binary crack detection map. (c) Corresponding crack roughness image.

sliding-window version of the Radon transform is applied to the airborne F-SAR datasets. These investigations are detailed in the following two sub-sections.

A. Investigations using simulated road crack images

To evaluate the capability of the Radon transform in estimating crack severity and orientation, a series of 5 × 5 noisy images was generated to simulate road cracks at different orientations. Each image contains random background noise and a single line oriented at a specified angle relative to the x-axis, resembling how cracks appear in SAR backscatter or surface roughness (h_{rms}) images. The use of 5 × 5 images is intentional, as the Radon transform is applied locally in real SAR data using a sliding window. It is therefore important to assess whether the transform remains effective when limited to only 25 input pixels within a 5×5 window. For the X-band F-SAR data used in this study, which has a spatial resolution of 0.25 m, a 5×5 window corresponds to an area of approximately 1.25×1.25 meters on the road surface.

Fig. 4 shows the simulated cracks oriented at 0, 20, 45, and 70 degrees along with their corresponding Radon sinograms and magnitude plots. The sinogram provides a two-dimensional representation of the Radon output, where the x-axis denotes the Radon projection angle (θ_{r}) and the y-axis represents the distance from the origin along each projection line. Analysis of these sinograms reveals that the maximum Radon magnitudes occur at angles matching the actual orientations of the simulated cracks. Therefore, in this study, the angle corresponding to the maximum Radon magnitude is interpreted as the estimated crack orientation, while the

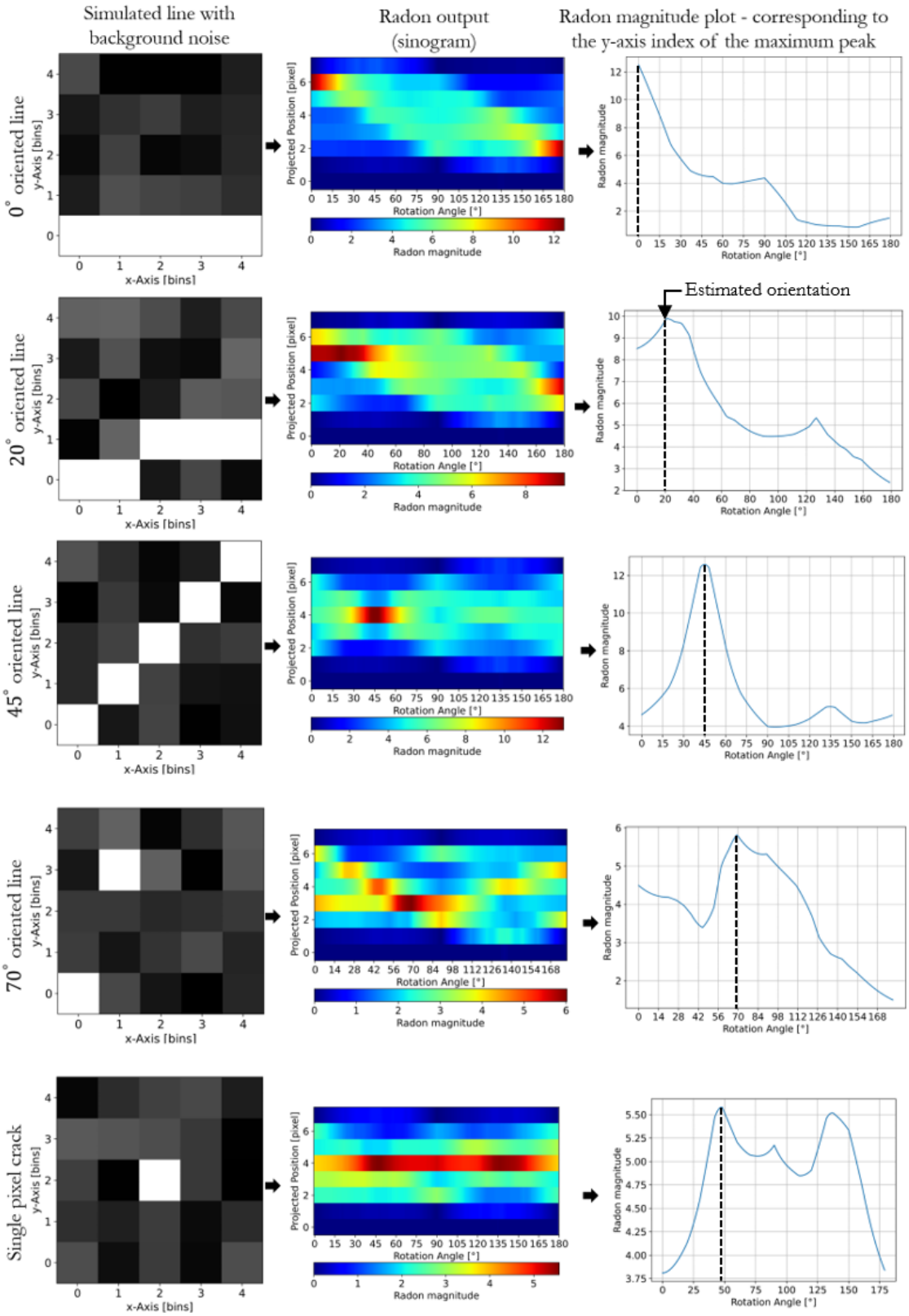

Fig. 4. Crack detection, severity, and orientation estimation results using simulated lines with background noise resembling crack in a SAR backscatter image.

maximum Radon magnitude value itself is used as a qualitative measure of the crack severity. This relationship is further confirmed by the Radon magnitude plots, which are extracted along the y-axis index of each sinogram at its maximum response. These plots clearly show that the Radon peaks align with the known crack angles. Notably, even in the case of the

70-degree-oriented crack, which is represented by only two pixels, the correct orientation is accurately estimated by the Radon transform.

To explore the limitations of this method, an additional experiment was conducted using a 5 × 5 image containing only a single-pixel crack. As shown in the last row of Fig. 4, the Radon transform does not produce a clear peak in this case, and the resulting orientation estimate is inaccurate. This indicates that a crack must span at least two pixels within the window for reliable orientation and severity estimation. Furthermore, when multiple isolated single-pixel cracks are present, the Radon transform may incorrectly interpret them as a single crack, leading to erroneous severity and orientation estimates.

In summary, the results from Fig. 4 demonstrate that the Radon transform can effectively estimate crack orientation and provide a qualitative measure of severity when the crack covers at least two pixels. However, since the Radon transform generates an output regardless of whether a crack is present, it should only be applied to pre-processed images where cracks have already been detected, such as the crack roughness image produced by the adaptive thresholding algorithm (cf. Section III).

B. Application of windowed Radon transform on the crack roughness image generated from adaptive thresholding

A dedicated processing chain has been developed to estimate the crack severity and orientation from X-band F-SAR data, based on the previously described principle of the maximum Radon magnitude and its corresponding projection angle. This method takes as input the crack roughness image produced by the adaptive thresholding algorithm (cf. Section III). The complete workflow is illustrated in Fig. 5.

Within this processing chain, the Radon transform is applied locally to the large crack roughness image using a 5×5 sliding window. As demonstrated previously with the simulated cracks in Fig. 4, a 5×5 window provides sufficient pixels for reliable severity and orientation estimation using the Radon transform. Using a larger window could cause multiple cracks to overlap, resulting in missing out smaller cracks and blurred outputs. In addition, the sliding window is moved across the input image in an overlapping manner, increasing the likelihood of detecting cracks that might be missed in the current position but detected in the next slightly shifted position of the sliding window.

This overlapping shifting of the sliding window is particularly useful in cases where multiple cracks of varying severities fall within a single 5×5 window ($1.25\,\mathrm{m} \times 1.25\,\mathrm{m}$ on the road surface for the input F-SAR data). In such scenarios, the maximum magnitude of the Radon sinogram typically points only to the most prominent crack in the window. As each window is shifted by one pixel (approx. 25 cm on the ground for the F-SAR data), cracks that may have produced lower peaks in the Radon sinogram in the previous position can become more centrally located in the next, thereby increasing their chances of detection by producing a stronger peak. While very fine or narrow crack segments may still go undetected,

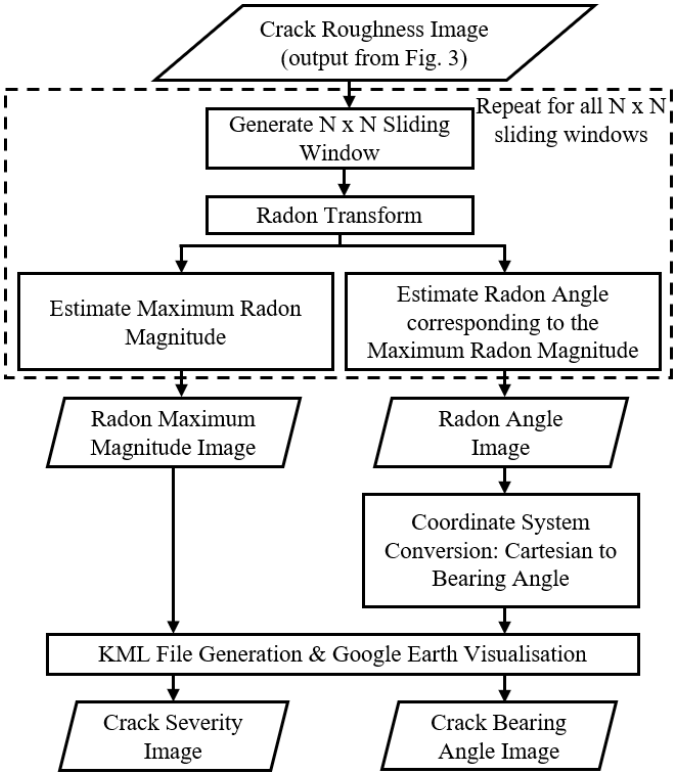

Fig. 5. Block diagram of the windowed Radon transform-based processing chain for crack severity and orientation estimation.

this overlapping strategy significantly enhances the likelihood of identifying the more severe portions of longer, closely located cracks that may span over multiple sliding windows.

At each window position, the Radon transform calculates the maximum Radon magnitude and the corresponding projection angle (θ_r). These values are recorded across the entire image to produce two outputs: a Radon maximum magnitude image, which provides a qualitative measure of the crack severity, and a Radon angle image, which captures the orientation of cracks. The Radon maximum magnitude image is then used to generate a KML file for visualizing the crack severity in GE, while the Radon angle image is further processed to estimate the orientation of cracks.

The Radon angle image represents the orientation angles (θ_r) of the detected cracks in the Cartesian coordinate system measured w.r.t. the x-axis. However, for a geospatially meaningful interpretation, these angles must be converted into bearing angles (θ_b), which are referenced to true north. This conversion is carried out using the following equation:

$$\theta_\mathrm{b} = (90^\circ - \theta_\mathrm{r} - \theta_\mathrm{road} - \theta_\mathrm{decl}) \bmod 360^\circ\,, \tag{3}$$

where θ_road denotes the road orientation angle relative to true north, estimated from the OpenStreetMap (OSM) data, and θ_decl is the grid declination angle, which accounts for the difference between UTM grid north and true north [35]. This correction is necessary because the Radon transform is applied to geocoded images in the UTM coordinate system.

Following this coordinate transformation, the Radon angle image expressed in the bearing angle system is used to

generate a second KML file that visualizes the orientation of the detected cracks in Google Earth.

The chances of false crack detections are also minimal in this approach. Since the Radon transform operates only on the crack roughness image generated by the adaptive thresholding algorithm, all smooth or background regions have already been set to zero. The Radon transform is thus applied only within the sliding windows containing non-zero values, which correspond to the cracks detected by the adaptive thresholding algorithm. This two-stage process minimizes the possibility of falsely detecting non-crack regions as cracks.

V. Experimental Results and Discussion

The crack detection, severity, and orientation estimation results generated from the X-band F-SAR datasets by applying the novel methods discussed in Sections III and IV are presented in the following sub-sections.

A. Flight heading angle dependency on cracks detection

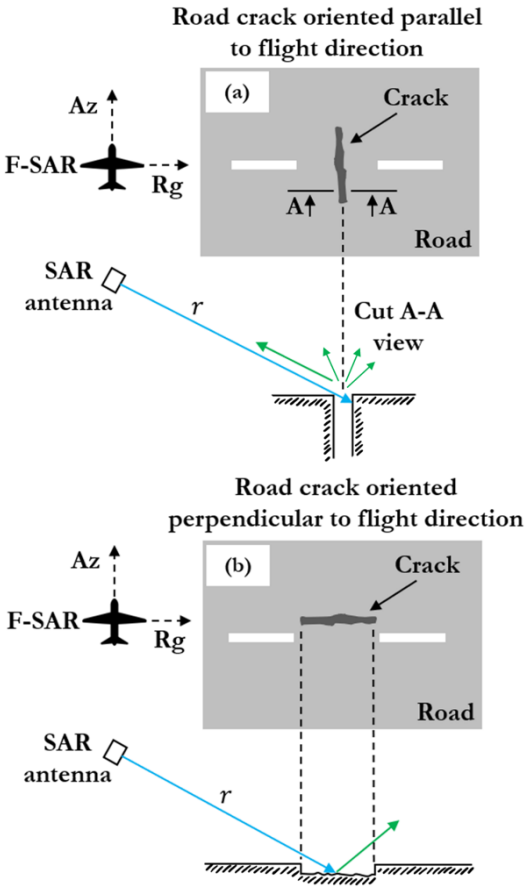

Fig. 6. Illustration of the flight heading angle dependency on the SAR backscatter response from a road crack. (a) Road crack oriented parallel to the flight direction. (b) Road crack oriented perpendicular to the flight direction.

Since road surface cracks are oriented line-like features, the flight heading angle of the airborne SAR system greatly influences their visibility in the acquired datasets. Fig. 6 shows an illustration demonstrating the flight heading angle dependency on the backscatter response from a road crack.

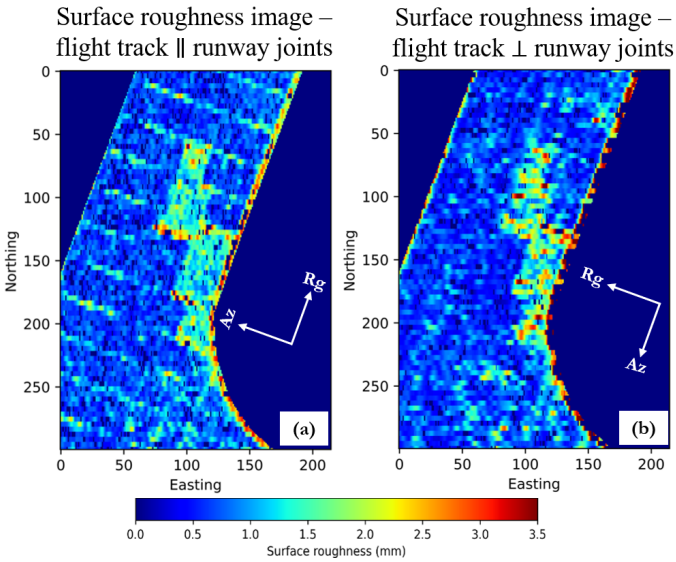

Fig. 7. Surface roughness (h_{rms}) images for the section of the Kaufbeuren runway generated from (a) PS05 dataset, (b) PS04 dataset.

Fig. 6(a) illustrates the data acquisition geometry for the F-SAR system when a road crack is oriented parallel to the flight direction. In this scenario, the SAR antenna, mounted on the side of the aircraft fuselage, illuminates the entire length of the crack from a direction perpendicular to the crack's orientation, resulting in a maximum backscatter response from the crack edges. Therefore, it is expected that the cracks are most visible in SAR images when the flight path is aligned with their orientation. In contrast, as shown in Fig. 6(b), if the flight direction is perpendicular or at an oblique angle to the crack, the radar signal cannot illuminate the entire length of the crack. Instead, most of the transmitted signal undergoes specular reflection from the inside of the crack instead of being backscattered from the crack edges. This leads to a reduced backscatter response and a diminished visibility of cracks in the SAR images, potentially causing an underestimation of the severity of the cracks.

In Fig. 7(a), the h_{rms} image for a section of the Kaufbeuren runway is shown, corresponding to the area displayed in the GE and the expected cracks images in Fig. 2(a) and (b), respectively. This image is generated with the PS05 F-SAR dataset with a flight track perpendicular to the runway (see azimuth and range direction arrows). Here, the flight track is parallel to the small joints present across the runway, resulting in a strong backscatter response and making these joints visible as regions of high surface roughness. Conversely, Fig. 7(b) shows the h_{rms} image generated from the PS04 F-SAR dataset, having its flight track perpendicular to the orientation of these small joints, rendering them invisible. This demonstrates that the flight heading angle significantly affects the detectability of cracks in airborne SAR data acquired along linear flight tracks, confirming the backscattering assumptions based on the crack orientations shown in Fig. 6. Thus, the flight heading angle is crucial for crack detection, and the airborne SAR data should be acquired with a flight (azimuth) track parallel to the orientation of the cracks of interest to ensure their visibility.

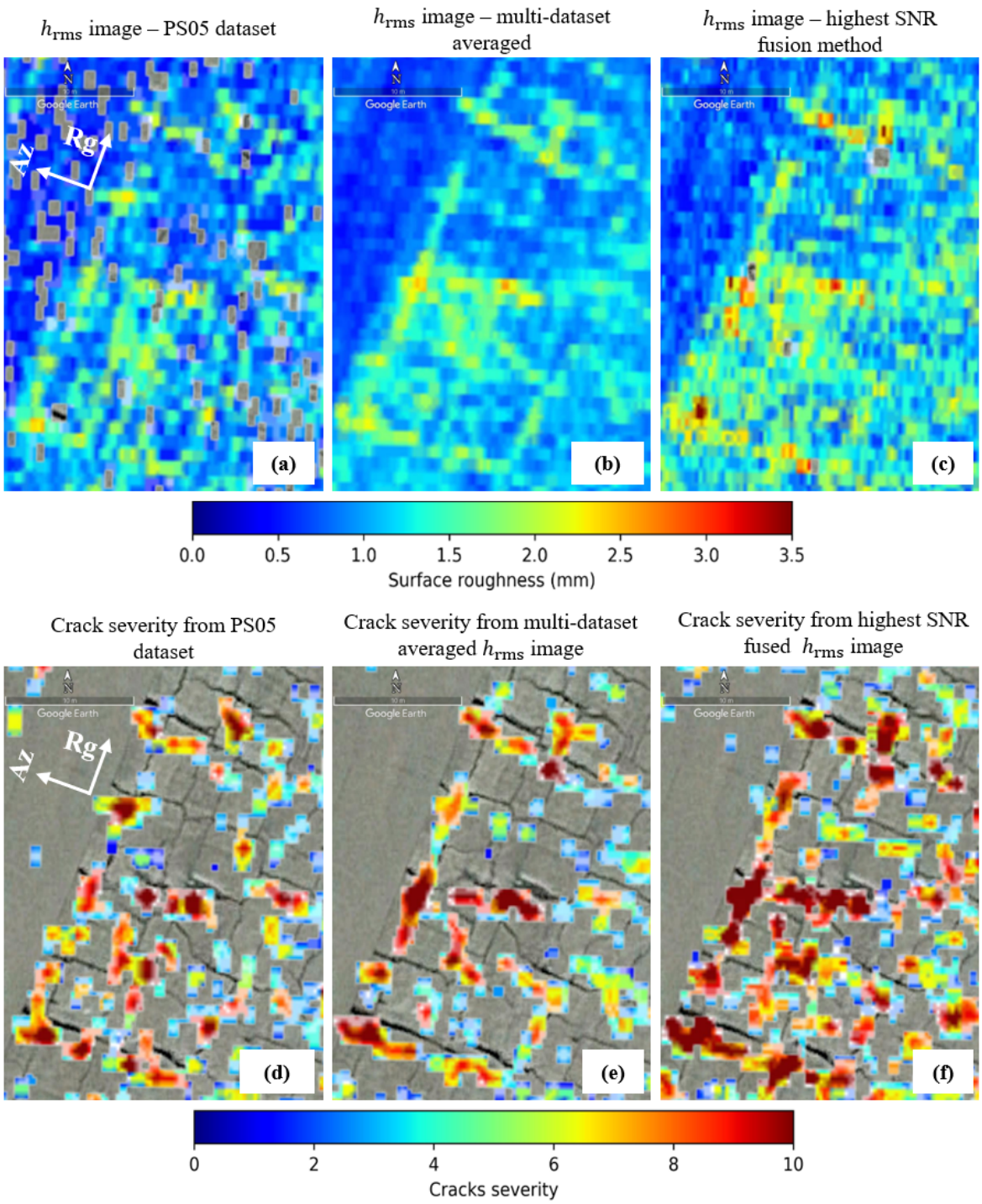

Fig. 8. Crack detection results generated for the section of the Kaufbeuren parking area marked as 'Detail 1' in Fig. 2(c). Surface roughness images used as input for cracks detection generated from (a) PS05 dataset (grey spots indicate masked-out areas with invalid h_{rms} values [16]), (b) multi-dataset averaging, and (c) highest SNR method. The corresponding crack severity images are presented in (d)–(f), respectively (offsets between the detected cracks and the underlying GE imagery are due to residual geocoding errors in range direction).

B. Cracks detection results

Fig. 8 shows the GE visualizations of crack detection and severity estimation results for the Kaufbeuren parking area section labeled 'Detail 1' in Figs. 2(c) and (e), using the combined adaptive thresholding and Radon transform approach. h_{rms} images generated from the PS05 dataset, multi-dataset averaging, and highest SNR methods are shown in Fig. 8(a), (b), and (c), respectively. The corresponding crack severity images are presented in Fig. 8(d), (e), and (f). The grey spots in Fig. 8(a) indicate masked-out areas with invalid h_{rms} values [16]. Across all cases, areas with elevated surface roughness values correspond well to the detected cracks, which closely match the cracks visible in the underlying GE imagery. Larger cracks are shown in yellow to red, indicating higher severity,

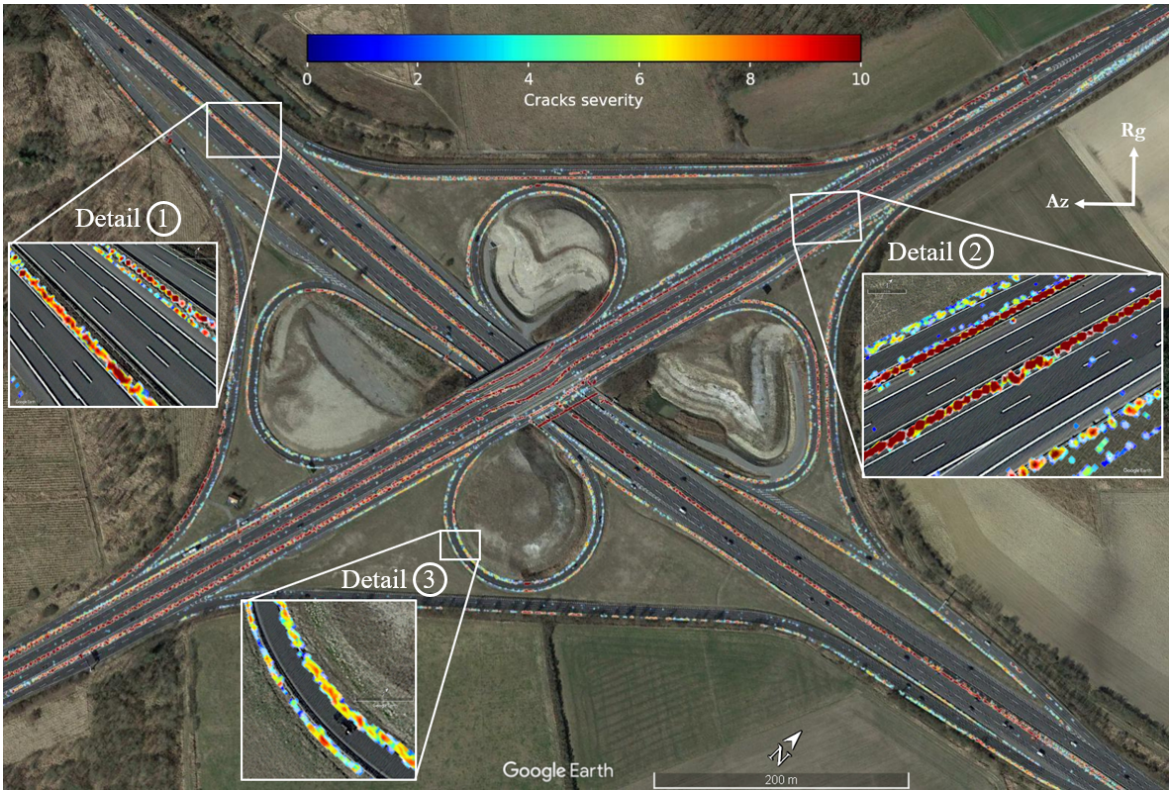

Fig. 9. Google Earth visualization of the crack severity image generated for the Wolfsburg motorway intersection at Braunschweig, Germany.

while smaller cracks appear in cyan to green, indicating lower severity. The number of detected cracks varies depending on the input image due to the influence of flight heading angle on crack visibility, as discussed in Section V-A. The result in Fig. 8(d), derived from the PS05 dataset input, shows more detected cracks than Fig. 8(e), which uses the fused h_{rms} image generated from the multi-dataset averaging method as input, where minor cracks are smoothed out due to the averaging process. Fig. 8(f), based on the highest SNR fused h_{rms} image input, detects the highest number of cracks due to the enhanced sensitivity of this method to local backscatter variations; however, this comes at the cost of a grainier input h_{rms} image and an increased likelihood of false detections. These results suggest that generating multiple crack severity images from individual SAR acquisitions with different flight heading angles provides more reliable detection of cracks with varying orientations than using fused h_{rms} images as input. Also, a slight positional offset can be observed between the detected cracks and the underlying GE imagery. This offset is most likely due to geocoding inaccuracies introduced by errors in the Digital Elevation Model (DEM) used for geocoding and terrain correcting the SAR datasets. Since the proposed method operates on a single, already geocoded surface roughness image, no co-registration step is involved in the processing chain.

Since the previously discussed results were generated for a decommissioned runway section, an additional experiment was conducted to evaluate the performance of the crack detection and severity estimation method on an active road. For this purpose, F-SAR data were acquired over the Wolfsburg motorway intersection in Braunschweig, Germany, which features a smooth, crack-free road surface. Fig. 9 presents the resulting crack severity image, where only unmasked features such as road borders, flyover walls, and metallic lane dividers are detected as cracks due to their high backscatter (σ^o) values, with road borders appearing from cyan to red and lane dividers mostly in red. It should be noted that the upper σ^o thresholding mentioned in Section III was intentionally not applied to the h_{rms} image for this test site. Consequently, these high-backscatter structures were falsely identified as cracks. This highlights the importance of performing the upper σ^o thresholding procedure prior to crack detection. Apart from a few isolated blue pixels (cf. Detail ② in Fig. 9), no cracks are detected on the actual road surface, which is consistent with the underlying GE imagery. These results demonstrate that the combined adaptive thresholding and Radon transform approach can effectively detect real cracks without significant false positives on smooth road surfaces.

C. Cracks orientation estimation results

Fig. 10 displays the cracks orientation estimation results for the section of the Kaufbeuren parking area marked as 'Detail 1' in Fig. 2(c) and (e). h_{rms} images generated from the PS05 dataset, multi-dataset averaging, and highest SNR methods are shown in Fig. 10(a), (b), and (c), respectively. The corresponding crack bearing angle images are presented in Fig. 10(d), (e), and (f). By comparing these input h_{rms} images with the crack bearing angle images, it can be seen that

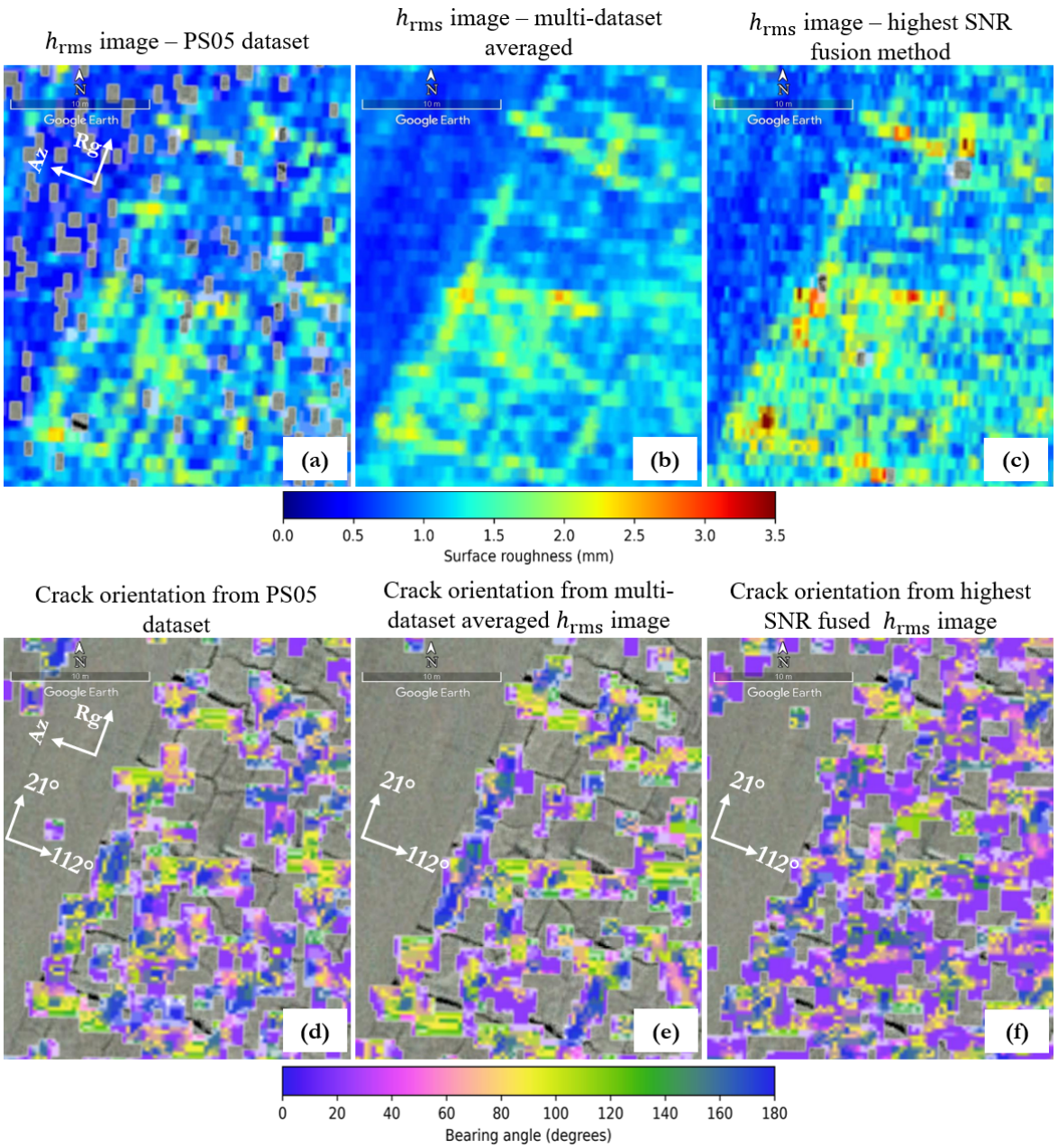

Fig. 10. Crack orientation estimation results generated for the section of the Kaufbeuren parking area marked as 'Detail 1' in Fig. 2(c). Surface roughness images used as input for the cracks orientation estimation generated from (a) the PS05 dataset (grey spots indicate masked-out areas with invalid h_{rms} values [16]), (b) multi-dataset averaging, and (c) the highest SNR method. The corresponding crack bearing angle images are presented in (d)–(f), respectively (offsets between the detected cracks and the underlying GE imagery are due to residual geocoding errors in range direction).

the cracks along the north-east direction predominantly appear in purple, indicating a bearing angle of around 20 degrees, while the cracks aligned in the east-south direction appear in yellow to green, indicating a bearing angle of around 115 degrees. In all three images, the bearing angles estimated by the Radon transform-based method closely match the actual bearing angles of the cracks measured from GE, as indicated by the white arrows. However, the number of detected cracks varies depending on the h_{rms} image used as input. The main cracks visible in the GE image are accurately detected from the PS05 dataset, while the number of detected cracks is less when the multi-dataset averaged h_{rms} image is used as input. The crack bearing angle image generated from the highest SNR fused h_{rms} image shows a large number of cracks in this region, which can be false crack detections due to the grainy/noisy appearance of the h_{rms} image. Therefore, the multi-dataset averaged and the highest SNR method-based h_{rms} images are not recommended for crack detection and orientation estimation. As already pointed out, the best approach will be to generate multiple crack bearing angle images from individual SAR datasets that have different flight heading angles.

Fig. 11 shows the histograms for the crack bearing angle images discussed in Fig. 10 for the section of the Kaufbeuren

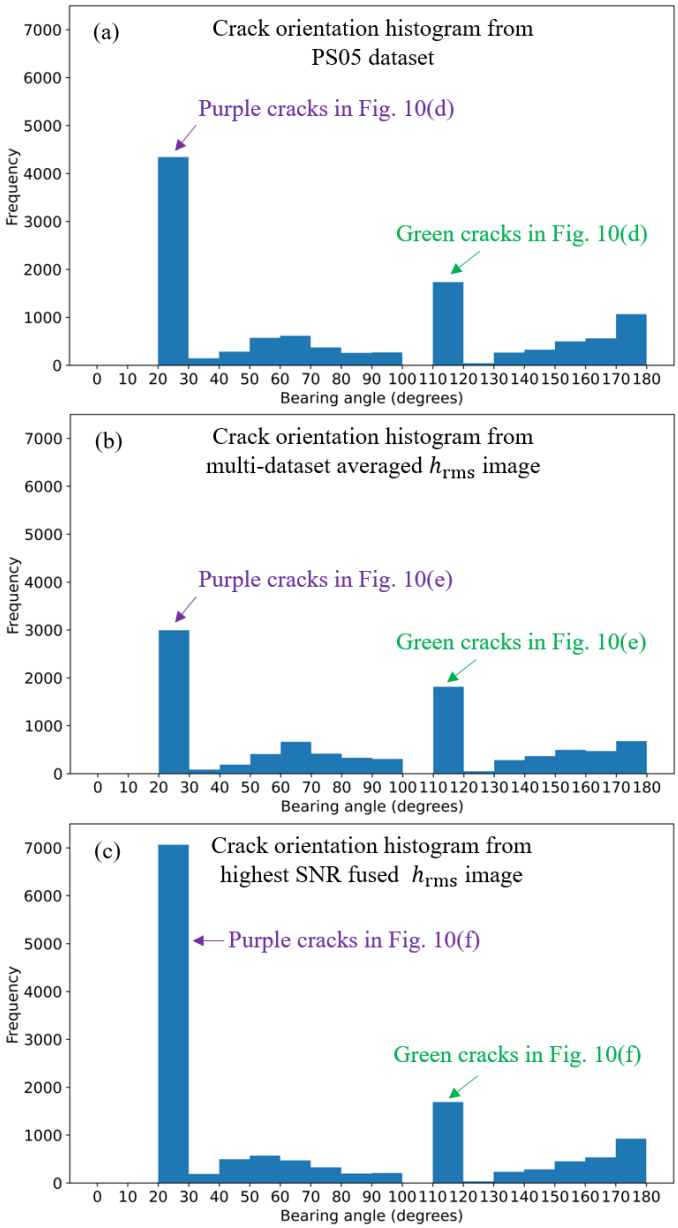

Fig. 11. Histograms for the crack bearing angle images shown in Fig. 10 for the section of the Kaufbeuren parking area. Generated from (a) PS05 dataset, (b) multi-dataset averaging, and (c) highest SNR method-based input h_{rms} images.

parking area. Specifically, Fig. 11(a) presents the histogram from the PS05 dataset, (b) from the multi-dataset averaging method, and (c) from the highest SNR method. All three histograms indicate that the dominant bearing angles are in the ranges of 20 to 30 degrees and 110 to 120 degrees. The 20 to 30 degrees range corresponds to the purple-colored cracks, which match the GE-measured ground truth value of 21 degrees. The 110 to 120 degrees range corresponds to the green-colored cracks, matching the ground truth value of 112 degrees. As discussed previously, the number of detected cracks varies depending on the h_{rms} image used as input. These histograms demonstrate that the crack bearing angles estimated by the Radon transform-based method are in close agreement with the ground truth bearing angles measured from GE.

Therefore, from the crack severity, crack bearing angle, and histogram images presented in this section, it can be concluded that the combined adaptive thresholding and Radon transform-based method is a reliable approach for detecting and estimating the severity and orientation of cracks on the road surface.

VI. Conclusion

This article proposes a novel methodology for road cracks detection and orientation estimation using high-resolution SAR data acquired by the airborne X-band F-SAR system. Analysis of the surface roughness images from different F-SAR datasets showed that crack visibility in SAR images depends on the flight heading angle due to the oriented nature of cracks. Therefore, the flight heading angle for the crack detection and orientation estimation should be chosen based on the orientation of the cracks of interest, such as longitudinal or transverse cracks. SAR data acquisition with a flight track parallel to the crack orientation ensures the best visibility of the crack in the SAR backscatter and surface roughness images. A combined approach using an adaptive thresholding algorithm and the Radon transform has been proposed in this study, which successfully detected the cracks and estimated their severity and orientation, with results validated using GE. The Radon magnitude values were used to colour-code the detected cracks, showing their severity from minor to severe, and the estimated orientation angles closely agreed with the measurements from GE. Fused surface roughness images produced by multi-dataset averaging or the highest SNR method are not ideal to be used as input images for crack detection, as they may either miss smaller cracks or produce many false detections. The most effective input for accurate crack detection and orientation estimation is a surface roughness image generated from a single F-SAR dataset. However, cracks with certain orientations might remain undetected if they are not well-visible in this single dataset. To address this limitation, it is recommended to generate multiple crack detection and orientation estimation results using several F-SAR datasets acquired with different flight heading angles. Specifically, at least two flight heading angles should be used: one parallel and one perpendicular to the road. This will help in detecting both longitudinal and transverse cracks, which are common on road surfaces. The use of a future very-high-resolution airborne Ka-band SAR system can improve the sensitivity of the cracks detection algorithm to smaller cracks on the road surface because of its higher sensitivity to road surface changes. Such a system is currently under development at the Microwaves and Radar Institute of the German Aerospace Center (DLR). As part of future work, post-processing strategies such as clustering of the detected crack pixels can be explored to extract higher-level features such as individual crack length, width, and spatial patterns. These metrics will be valuable for quantitative damage assessment and for prioritizing road maintenance efforts. In addition, future work will benefit from the availability of very detailed ground-truth data collected

using specialized road survey vehicles. A joint campaign was recently conducted in Germany by DLR in cooperation with a road condition monitoring company, where high-resolution X-band F-SAR data were acquired in parallel with survey vehicle measurements over a long motorway stretch. This forthcoming survey vehicle data will provide the precise ground truth needed to compute quantitative performance metrics, such as crack detection rate and false alarm rate, enabling more rigorous validation of the proposed methodology. These analyses, together with advanced post-processing strategies, will form the focus of a follow-on IEEE journal publication.

REFERENCES

[1] M. A. Afridi, S. Erlingsson, and L. Sjögren, "Municipal street maintenance challenges and management practices in Sweden," *Frontiers in Built Environment*, vol. 9, 2023.

[2] P. Lavin, *Asphalt pavements: a practical guide to design, production and maintenance for engineers and architects*. CRC Press, 2003.

[3] Y. Pan, X. Zhang, G. Cervone, and L. Yang, "Detection of asphalt pavement potholes and cracks based on the unmanned aerial vehicle multispectral imagery," *IEEE Journal of Selected Topics in Applied Earth Observations and Remote Sensing*, vol. 11, no. 10, pp. 3701–3712, 2018.

[4] R. Agrawal, Y. Chhadva, S. Addagarla, and S. Chaudhari, "Road surface classification and subsequent pothole detection using deep learning," in *2021 2nd International Conference for Emerging Technology (INCET)*, 2021, pp. 1–6.

[5] M. A. Alsheyab, M. A. Khasawneh, A. Abualia, and A. Sawalha, "A critical review of fatigue cracking in asphalt concrete pavement: a challenge to pavement durability," *Innovative Infrastructure Solutions*, vol. 9, no. 10, p. 386, Sep 2024.

[6] S. S. Adlinge and A. Gupta, "Pavement deterioration and its causes," *International journal of innovative research and development*, vol. 2, no. 4, pp. 437–450, 2013.

[7] S. Y. Amakye, S. J. Abbey, and C. A. Booth, "Road pavement defect investigation using treated and untreated expansive road subgrade materials with varying plasticity index," *Transportation Engineering*, vol. 9, p. 100123, 2022.

[8] A. F. Ikechukwu and M. M. Hassan, "Assessing the extent of pavement deterioration caused by subgrade volumetric movement through moisture infiltration," *International Journal of Pavement Research and Technology*, vol. 15, no. 3, pp. 676–692, May 2022.

[9] M. R. Islam and R. A. Tarefder, "Quantifying traffic- and temperature-induced fatigue damages of asphalt pavement," *Transportation Infrastructure Geotechnology*, vol. 2, no. 1, pp. 18–33, Mar 2015.

[10] A. Arabzadeh and M. Guler, "Thermal fatigue behavior of asphalt concrete: A laboratory-based investigation approach," *International Journal of Fatigue*, vol. 121, pp. 229–236, 2019.

[11] M. Arabani, S. Mirabdolazimi, and A. Sasani, "The effect of waste tire thread mesh on the dynamic behaviour of asphalt mixtures," *Construction and Building Materials*, vol. 24, no. 6, pp. 1060–1068, 2010.

[12] S. Alshammari, H. Gebre-Amlak, K. Ayinala, S. Song, and B.-Y. Choi, "Optimizing city's service routes for road repairs," in *2020 IEEE International Smart Cities Conference (ISC2)*, 2020, pp. 1–8.

[13] D. M. Hershfield, "Freeze-thaw cycles, potholes, and the winter of 1977–78," *Journal of Applied Meteorology (1962-1982)*, vol. 18, no. 8, pp. 1003–1007, 1979.

[14] C. Grégoire, A. V. d. Wielen, C. V. Geem, and J.-P. Drevet, "Methodologies for the use of ground-penetrating radar in road condition surveys," Belgian Road Research Centre, Tech. Rep., 2016.

[15] J. Laurent, D. Lefebvre, and E. Samson, "Development of a new 3d transverse laser profiling system for the automatic measurement of road cracks," in *Symposium on Pavement Surface Characteristics, 6th, 2008, Portoroz, Slovenia*, 2008.

[16] A. Babu, S. V. Baumgartner, and G. Krieger, "Approaches for road surface roughness estimation using airborne polarimetric SAR," *IEEE Journal of Selected Topics in Applied Earth Observations and Remote Sensing*, vol. 15, pp. 3444–3462, 2022.

[17] E. Parliament, D.-G. for Internal Policies of the Union, A. Stanghellini, R. Frisoni, R. Lidia, J. Neri, T. Sawicki, L. Devenish, L. Casullo, S. Carl, C. Vollath, R. Silaghi, F. Spano, and F. Dionori, *EU road surfaces : economic and safety impact of the lack of regular road maintenance*. Publications Office, 2014.

[18] M. I. Bani Baker, R. M. Abendeh, and M. A. Khasawneh, "Freeze and thaw effect on asphalt concrete mixtures modified with natural bentonite clay," *Coatings*, vol. 12, no. 11, 2022.

[19] E. Schnebele, B. F. Tanyu, G. Cervone, and N. Waters, "Review of remote sensing methodologies for pavement management and assessment," *European Transport Research Review*, vol. 7, no. 2, p. 7, Mar 2015.

[20] H. S. Munawar, A. W. A. Hammad, A. Haddad, C. A. P. Soares, and S. T. Waller, "Image-based crack detection methods: A review," *Infrastructures*, vol. 6, no. 8, 2021.

[21] E. El-Din Hemdan and M. E. Al-Atroush, "A review study of intelligent road crack detection: Algorithms and systems," *International Journal of Pavement Research and Technology*, May 2025.

[22] J. Zhu, J. Zhong, T. Ma, X. Huang, W. Zhang, and Y. Zhou, "Pavement distress detection using convolutional neural networks with images captured via uav," *Automation in Construction*, vol. 133, p. 103991, 2022.

[23] M. Zhang and J. Xu, "A semantic segmentation model for road cracks combining channel-space convolution and frequency feature aggregation," *Scientific Reports*, vol. 14, no. 1, p. 16038, Jul 2024.

[24] F. Ulaby, D. Long, and U. of Michigan. Press, *Microwave Radar and Radiometric Remote Sensing*. University of Michigan Press, 2014.

[25] W. Suanpaga and K. Yoshikazu, "Riding quality model for asphalt pavement monitoring using phase array type L-band synthetic aperture radar (PALSAR)," *Remote Sensing*, vol. 2, no. 11, pp. 2531–2546, 2010.

[26] F. J. Meyer, O. A. Ajadi, and E. J. Hoppe, "Studying the applicability of X-Band SAR data to the network-scale mapping of pavement roughness on US roads," *Remote Sensing*, vol. 12, no. 9, 2020.

[27] S. Karimzadeh, M. Ghasemi, M. Matsuoka, K. Yagi, and A. C. Zulfikar, "A deep learning model for road damage detection after an earthquake based on synthetic aperture radar (sar) and field datasets," *IEEE Journal of Selected Topics in Applied Earth Observations and Remote Sensing*, vol. 15, pp. 5753–5765, 2022.

[28] L. G. Rischioni, A. Babu, S. V. Baumgartner, and G. Krieger, "Machine learning approaches for road condition monitoring using synthetic aperture radar," *IEEE Journal of Selected Topics in Applied Earth Observations and Remote Sensing*, vol. 16, pp. 3070–3082, 2023.

[29] A. Babu, D. Gerber, S. V. Baumgartner, and G. Krieger, "Road surface roughness estimation using spaceborne synthetic aperture radar," *IEEE Geoscience and Remote Sensing Letters*, vol. 20, pp. 1–5, 2023.

[30] L. A. Myers, R. Roque, B. E. Ruth, and C. Drakos, "Measurement of contact stresses for different truck tire types to evaluate their influence on near-surface cracking and rutting," *Transportation Research Record*, vol. 1655, no. 1, pp. 175–184, 1999.

[31] L. Zhou, F. Ni, and Y. Zhao, "Evaluation method for transverse cracking in asphalt pavements on freeways," *Transportation Research Record*, vol. 2153, no. 1, pp. 97–105, 2010.

[32] H. Cao, T. Chen, H. Zhu, and H. Ren, "Influence of frequent freeze–thaw cycles on performance of asphalt pavement in high-cold and high-altitude areas," *Coatings*, vol. 12, no. 6, 2022.

[33] S. R. Deans, *The Radon transform and some of its applications*. Courier Corporation, 2007.

[34] E. Trouvé, G. Mauris, J.-P. Rudant, E. Tonyé *et al.*, "Detection of linear features in synthetic-aperture radar images by use of the localized Radon transform and prior information," *Applied optics*, vol. 43, no. 2, pp. 264–273, 2004.

[35] U. S. A. M. Service, *Grids and Magnetic Declinations*, 1945, no. 425.